The Effects of Embedded Dipoles in Aromatic Self-Assembled Monolayers

Tarek Abu-Husein, Swen Schuster, David A. Egger, Martin Kind, Tobias Santowski, Adrian Wiesner, Ryan Chiechi, Egbert Zojer, Andreas Terfort,* and Michael Zharnikov**

Using a representative model system, here electronic and structural properties of aromatic self-assembled monolayers (SAMs) are described that contain an embedded, dipolar group. As polar unit, pyrimidine is used, with its orientation in the molecular backbone and, consequently, the direction of the embedded dipole moment being varied. The electronic and structural properties of these embedded-dipole SAMs are thoroughly analyzed using a number of complementary characterization techniques combined with quantum-mechanical modeling. It is shown that such mid-chain-substituted monolayers are highly interesting from both fundamental and application viewpoints, as the dipolar groups are found to induce a potential discontinuity inside the monolayer, electrostatically shifting the core-level energies in the regions above and below the dipoles relative to one another. These SAMs also allow for tuning the substrate work function in a controlled manner independent of the docking chemistry and, most importantly, without modifying the SAM-ambient interface.

1. Introduction

The control of physical and chemical properties of surfaces and interfaces is one of the most important issues of modern surface science, physical chemistry, and nanotechnology. Highly relevant systems in this context are self-assembled monolayers (SAMs), which are 2D polycrystalline films of semirigid molecules that are chemically anchored to a substrate by a suitable head group.[1,2] These systems have attracted considerable interest for more than three decades.[3] They have been used, e.g., for controlling wettability[4,5] or cell adhesion[6,7] and for corrosion protection.[8,9] They have also attracted considerable attention in the area of organic electronics, where they are, for example, used to modify gate dielectrics in organic transistors to enhance their performance,[10–12] to realize devices with novel functionalities such as memories[13] or sensors,[14] or even to act as the active layer of the device.[15] When bonded to electrodes, SAMs can be used to manipulate charge carrier injection barriers, to provide a better electronic coupling, and/or to act as an intermediate layer for the growth of the active organic material.[16–23]

The key issues in this context are (i) the conductive properties of the SAM itself, affecting the performance of the entire device, (ii) control of the SAM-ambient interface, defining the nucleation and growth mode of the organic semiconductor, and (iii) introduction of a specific dipole moment to manipulate charge carrier injection barriers. So far, characteristics of the SAM-ambient interface and adjustment of dipole moment were entangled since the common way to manipulate the entire electrostatic parameters of SAMs is the selection of a proper dipolar terminal tail group comprising the SAM-ambient interface.[24,25] This strategy, however, also affects the nucleation chemistry, making optimization of a particular system a highly difficult task.

While a system has recently been reported in which the mixing of two different, short molecules with almost opposing dipole moments led to layers with an adjustable dipole moment and unaltered surface energy,[22] a more general solution to this dilemma would be the incorporation of a suitable functional group into the backbone of the molecules forming the SAM such that a layer with buried dipole moments can be realized. This leaves further options for the independent optimization of the SAM-ambient interface, e.g., via suitable tail-group substitutions. Thus, the interfacial dipole and nucleation chemistry can be tuned separately, making it highly interesting for applications, e.g., when the SAM is used as intermediate, charge-injection promoting layer between a metal electrode and adjacent organic electronic material. In addition, one avoids having potentially reactive functional groups at the exterior of the SAM that could be

T. Abu-Husein, Dr. M. Kind, T. Santowski, A. Wiesner, Prof. A. Terfort
Institut für Anorganische und Analytische Chemie
Universität Frankfurt
Max-von-Laue-Straße 7, 60438 Frankfurt, Germany
E-mail: aterfort@chemie.uni-frankfurt.de

S. Schuster, Prof. M. Zharnikov
Angewandte Physikalische Chemie
Universität Heidelberg
Im Neuenheimer Feld 253, 69120 Heidelberg, Germany
E-mail: Michael.Zharnikov@urz.uni-heidelberg.de

Dr. D. A. Egger,[+] Prof. E. Zojer
Institute of Solid State Physics
NAWI Graz
Graz University of Technology
Petersgasse 16, 8010 Graz, Austria
E-mail: egbert.zojer@tugraz.at

Prof. R. Chiechi
Stratingh Institute for Chemistry and
Zernike Institute for Advanced Materials
University of Groningen
Nijenborgh 4, 9747 AG Groningen, The Netherlands

[+]Present address: Department of Materials and Interfaces, Weizmann Institute of Science, Rehovoth 76100, Israel

DOI: 10.1002/adfm.201500899

chemically modified during the growth of an organic film, which is clearly of advantage for the stability of the entire system. Beyond these practically relevant aspects, embedded groups can be used to introduce deliberately chosen chemical and physical perturbations within the monolayer. The extent of these perturbations can be precisely controlled by selectively choosing the functional dipolar moieties and the positions and orientations in which they are introduced within the chain. This opens up new and unique avenues for investigating fundamental aspects of SAM electrostatics and for designing SAMs with desired properties.

Embedding functional groups into SAMs has been a widely used strategy for obtaining additional functionalities, such as preferred cleaving[26–28] or providing (switchable) molecular dipole moments.[29] Nevertheless, these groups also had significant influence on the layer order, either by steric constraints[26,27,29] or by formation of intermolecular hydrogen bonds.[29] Recently, as a first attempt to build a system with embedded dipoles, ester groups, R—(C═O)—O—R′, were introduced into the alkanethiolate monolayer on gold as a representative test case.[30] In this system, indeed a variety of novel phenomena have been observed. From a fundamental point of view, the most interesting observation was a strong electrostatic effect in the X-ray photoelectron spectra. In the presence of embedded esters, the C 1s photoelectron kinetic energies were found to be consistently shifted by 0.85 eV between the chemically identical —(CH_2)— alkyl segments above and below the ester moiety, regardless of relative lengths of the segments. This shift correlates well with simple electrostatic estimates based on ester molecular dipoles. Notably, this observation, along with few others,[31–34] contradicts the generally accepted assumption that the photoemission spectra of SAMs can be described entirely within the general concept of a chemical shift.[35] As will be discussed in more detail below, this would indeed be the case for conductive samples but not for relatively poorly conducting organic layers of upright "standing" molecules that are in the focus of the present study. Further, it suggests that the electronic levels and the electrostatic potential distribution within a SAM can be controlled to a certain extent by the introduction of an embedded dipole layer.

In view of these promising findings and the potential applications, and based on theoretical predictions,[36] we present here a first study on aromatic SAMs that contain an embedded dipolar functional group. Note that aromatic monolayers are superior to aliphatic ones in terms of electrical conductance,[37–39] which makes them more suitable intermediate layers in organic electronics and photovoltaics assemblies. Also, these films are better suited as interfacial layers for the deposition of most organic semiconductors, which generally contain aromatic functional units.[40]

Here, we report a rational approach for adjusting the dipole moments without significantly altering the molecular structure or the interface chemistry. Starting from terphenyl-4-methanethiol C_6H_5—C_6H_4—C_6H_4—CH_2—SH (TP1), the monolayers of which on Au(111) are well investigated,[41–45] we substituted the central phenylene ring by a 2,5-pyrimidine group, in the two possible orientations (**Figure 1**). Since the pyrimidine group has a noticeable dipole moment (2.3 D),[46,47] this architecture allows for an arrangement of embedded dipoles pointing either upward or downward with respect to the substrate, assuming an upright molecular orientation. These SAM precursors are accordingly denoted as TP1-up and TP1-down, as shown in Figure 1. Their respective SAMs were characterized in detail by a number of complementary surface-analytical techniques, viz. X-ray photoelectron spectroscopy (XPS), high-resolution XPS (HRXPS), ellipsometry, infrared reflection absorption spectroscopy (IRRAS), near-edge X-ray absorption fine structure (NEXAFS) spectroscopy, and scanning tunneling microscopy (STM), to study the effect of embedded dipoles on the molecular organization and to ensure film quality and, thus, the reliability of our conclusions regarding the specific electrostatic effects of embedded dipoles. The latter effects were addressed by dedicated experimental tools and theoretical simulations.

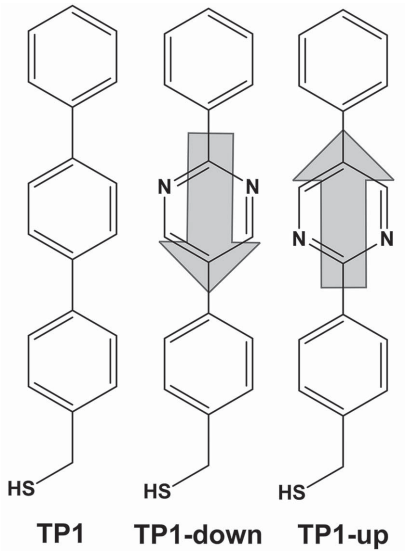

Figure 1. A schematic drawing of the pyrimidine-substituted molecules and major reference molecule along with their acronyms. The directions of the dipole moment associated with the embedded pyrimidine group are shown (the direction from the negative charge to the positive charge is considered as positive). The molecules are named accordingly. Individual rings will be named as ambient-adjacent, central, and substrate-adjacent ones, assuming an upright molecular geometry.

2. Results

2.1. Basic Characterization

2.1.1. XPS and HRXPS

Au $4f_{7/2}$, S 2p, and N 1s HRXP spectra of the TP1-down and TP1-up SAMs are presented in **Figure 2**, along with the data for the reference TP1 monolayer. The S 2p spectra of all three SAMs in Figure 2b exhibit a sole S $2p_{3/2,1/2}$ doublet at a binding energy (BE) position of ≈162.0 eV (S $2p_{3/2}$). This value corresponds to thiolate species bound to noble metal surfaces,[48–50] which means that, within the sensitivity of the measurements, all molecules in the studied films are bound to the substrate via a thiolate-gold bond, as is expected for well-defined SAMs. No traces of other sulfur-derived species such as atomic sulfur, disulfides, unbound thiols, or sulfonates were observed. The

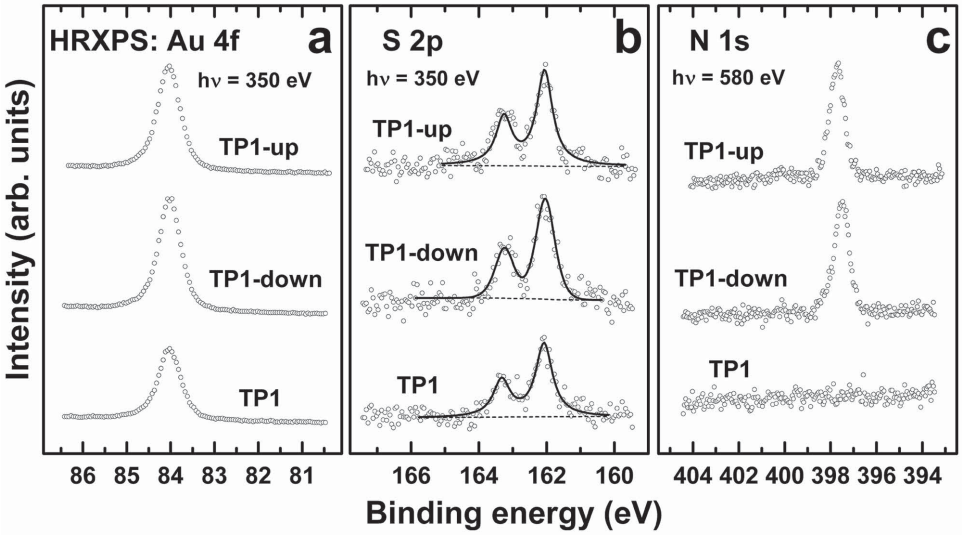

Figure 2. a) Au $4f_{7/2}$, b) S 2p, and c) N 1s HRXP spectra of the TP1, TP1-down, and TP1-up SAMs. The spectra were acquired at photon energies of 350 eV (Au $4f_{7/2}$ and S 2p) and 580 eV (N 1s). The S 2p spectra are fitted by a single S $2p_{3/2,1/2}$ doublet, characteristic of the thiolate.

TP1-down and TP1-up SAMs exhibit similar intensities of the S 2p signal, along with similar intensities of the Au $4f_{7/2}$ emission (Figure 2a), which suggest similar packing densities in these two monolayers. These densities appear, however, slightly lower than that in the TP1 SAM, as follows from the comparison of the Au $4f_{7/2}$ intensities in Figure 2a. This qualitative conclusion is supported by a numerical evaluation of the XPS and HRXPS data (see Section 5 for details), resulting in the values of effective thicknesses and packing densities compiled in **Table 1**. Note that the values for the reference TP1 monolayer agree well with the literature data.[44,45]

The N 1s HRXP spectra of the TP1-down and TP1-up SAMs in Figure 2c exhibit a single and sharp N 1s emission, in contrast to the expected, nitrogen-free "baseline" for the reference TP1 monolayer. This emission can be unequivocally assigned to the nitrogen atoms in the pyrimidine rings. The presence of the single and sharp peak suggests, in accordance with the S 2p data, a homogeneous and well-defined character of the target monolayers. Note that there is a small shift between the exact BE positions of the N 1s emissions for the TP1-down and TP1-up monolayers (397.5 and 397.7 eV, respectively).

The C 1s HRXP spectra of the TP1-down and TP1-up films are characteristic of well-defined SAMs. These spectra are, however, strongly affected by electrostatic effects. Thus, they will be described in detail below, when discussing the electrostatic properties of the SAMs.

Table 1. XPS/HRXPS and ellipsometry derived effective thickness of the TP1-down, TP1-up, and TP1 SAMs, along with the XPS/HRXPS derived packing density in these monolayers. The error bars of the packing density can be estimated at ±5%.

Monolayer	Effective thickness from XPS/HRXPS [nm]	Effective thickness from ellipsometry [nm]	Packing density [molecules cm^{-2}]
TP1	1.78 ± 0.04	1.80 ± 0.04	4.6×10^{14}
TP1-down	1.75 ± 0.05	1.80 ± 0.07	4.3×10^{14}
TP1-up	1.74 ± 0.05	1.73 ± 0.06	4.2×10^{14}

2.1.2. Ellipsometry

The film thickness values derived from the ellipsometry data are also presented in Table 1 and agree well with the XPS/HRXPS-derived values. The effective thicknesses of the TP1-down and TP1-up SAMs are, on average, slightly lower than that of the reference TP1 monolayer, corroborating the XPS/HRXPS data that suggest lower effective packing densities in these films.

2.1.3. IR Spectroscopy

IR spectra of TP1, TP1-down, and TP1-up SAMs are displayed in **Figure 3**, along with the spectra of the respective precursors and the results of the density functional theory (DFT) calculations for the isolated molecules. The assignments of the most prominent vibrational modes for the TP1-down and TP1-up monolayers are compiled in **Table 2**; analogous data for the TP1 SAM are presented in Table S1 (Supporting Information) and can also be found in the literature.[45] When comparing the experimental spectra of the neat substances with the IRRA spectra of the respective SAMs, it becomes evident from the band assignments (Table 2 and S1, Supporting Information) and the spectra in Figure 3 that vibrational modes with transition dipole moments (TDMs) parallel to the molecular backbone (labeled as "∥") remain intense, while the bands with perpendicular TDMs (either in plane of the aromatic rings, designated as "⊥," or out of this plane, assigned as "oop") are clearly attenuated in comparison to the relative strengths found in the bulk spectra.

In view of the surface selection rules for metal substrates,[51] this suggests an upright molecular orientation in all studied

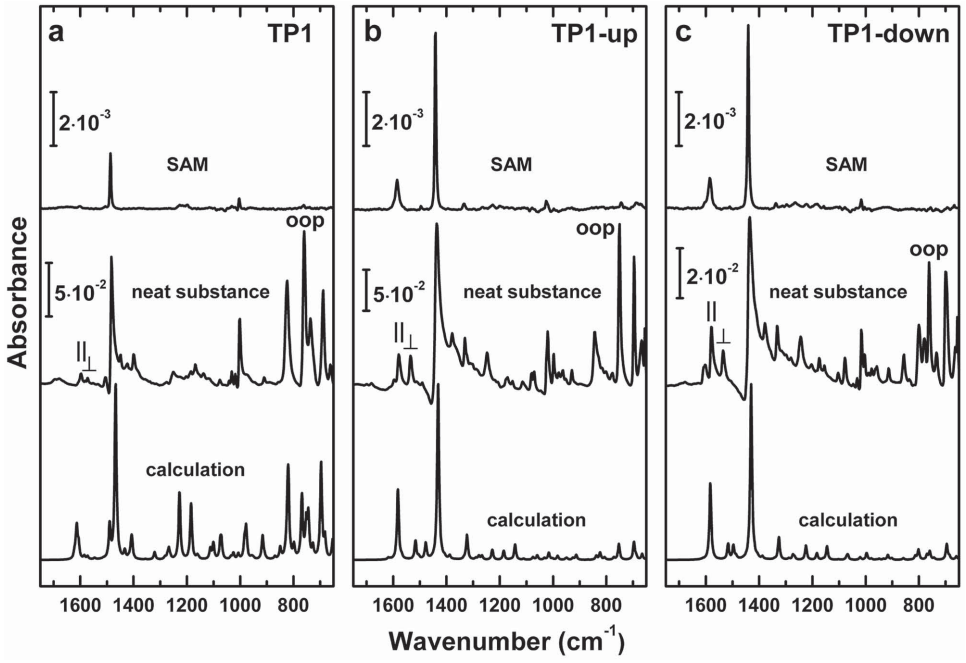

Figure 3. IRRA spectra of the a) TP1, b) TP1-up, and c) TP1-down SAMs (upper curves) along with the attenuated total reflection (ATR) IR spectra of the neat substances (middle curves) and the DFT calculated spectra (bottom curves). For the experimental spectra, absorbance scale bars are given. The spectra of the SAMs are plotted with identical scaling. The calculated spectra are displayed in arbitrary units. The orientations of some modes with respect to the molecular backbone are marked.

SAMs, which is in line with the thicknesses of these monolayers determined by XPS and ellipsometry. Beyond these qualitative considerations, numerical evaluation of the IR data was performed. With intensities of IR bands with three independent TDM directions at hand, the tilt and twist angles of the molecular adsorbates on a gold substrate can be calculated,[52] as has been done, e.g., for alkanethiolate SAMs on gold.[53] Note that the tilt angle, β, describes the deviation of the direction of the molecular backbone from the surface normal while the twist angle, γ, defines rotation about the molecular axis (at $\gamma = 0$, the TDMs of oop-modes lie in the plane spanned by the surface normal and the 4,4′-axes).[54] For the TP1-down and TP1-up monolayers, comparison of the intensities of bands **2** (oop), **6** (⊥), and **7** (∥) yields tilt angles of 12° and 18° and twist angles of 28° and 37°, respectively, though with relatively large error bars (±5°) due to low intensities of the ⊥ and oop bands. This problem was exacerbated for the TP1 SAM to the extent that the values of β and γ could not be derived. Note also that this discussion and the evaluation of tilt and twist angles assume that the three aromatic rings are coplanar. This assumption is based on the fact that the dihedral rotation typical of biphenyls and terphenyls in the molecular state (≈40°)[55,56] is strongly reduced or even eliminated completely in densely packed 2D assemblies due to intermolecular interactions,[57–60] as supported by the literature data[61,62] and corroborated, in this case, by the NEXAFS results discussed next.

Table 2. Positions (given in cm^{-1}) and assignments of most prominent vibrational modes in the IR spectra of the TP1-down and TP1-up molecules and the respective SAMs, along with the respective theoretical values (DFT) and TDM orientation.

			TP1-down			TP1-up		
No.	Mode[a)]	TDM[b)]	DFT	Neat[c)]	SAM[c)]	DFT	Neat[c)]	SAM[c)]
1	γCH ring twist	oop	696	696 s		696	699 s	
2	γCH ring twist	oop	753	751 vs	743 vw	759	762 s	
3	νCC	∥	1016	1021 m	1025 w	1021	1015 m	1018 w
4	νCC δCH	∥	1323	1330 m	1334 w	1326	1331 m	1337 w
5	νCC δCH	∥	1431	1437 vs	1441 vs	1430	1435 vs	1441 vs
6	νCC CN δCH	⊥	1516	1534 m	1534 vw	1516	1535 m	1535 vw
7	νCN δCH	∥	1582	1579 m	1586 m	1583	1579 m	1585 m

[a)] ν: stretch mode, δ: in-plane bending mode, γ: out of plane bending mode; [b)] ∥: parallel to main molecular backbone, ⊥: perpendicular to main molecular backbone and in plane of the aromatic rings, oop: perpendicular to the aromatic ring plane; [c)] vs: very strong, s: strong, m: medium, w: weak, vw: very weak.

2.1.4. NEXAFS Spectroscopy

The carbon and nitrogen K-edge NEXAFS spectra of the TP1, TP1-down, and TP1-up SAMs are presented in **Figure 4**. Panels (a) and (c) compile the spectra acquired at an X-ray incidence angle of 55° while panels (b) and (d) represent the difference between the spectra acquired at X-ray incident angles of 90° and 20°. Note that 55° is the so-called "magic angle;" at this particular adjustment, the spectrum is not influenced by any effects related to molecular orientation and is, therefore, exclusively representative of the chemical composition of the samples.[63] In contrast, the difference of the spectra acquired at normal (90°) and grazing (20°) incidence of X-rays is a fingerprint of the linear dichroism and, thus, allows conclusions regarding the orientational order and molecular orientation in the systems.

The 55 °C K-edge spectrum of the reference TP1 monolayer in Figure 4a exhibits the typical absorption signature of oligophenyls, in good agreement with the literature data.[44] The spectrum is dominated by the intense π_1^* resonance of the phenyl rings (**1**) at 284.95 eV, accompanied by the respective π_2^* peak (**3**) at ≈288.8 eV, and several σ^* resonances (**4–6**) at higher excitation energies.[63–66] In addition, there are the R*/C—S* resonance (**2**) at ≈287.0 eV[44,66] and a weak R* feature at ≈287.8 eV (between **2** and **3**).

Apart from certain intensity differences, the spectra of the TP1-down and TP1-up SAMs exhibit similar resonance patterns (**2–6**) at high photon energies (PEs) as the TP1 monolayer. At the same time, the dominant π_1^* resonance splits in three lines at PEs of 284.85/285.0 eV (**1a** for TP1-down/TP1-up), 285.3 eV (**1b**), and 286.0 eV (**1c**), which is more obvious for TP1-down/Au. This splitting is associated with the effect of the embedded pyrimidine moiety. Indeed, a NEXAFS spectrum of the pyrimidine molecule is dominated by a split π^* resonance at PEs of 285.32 and 285.86 eV related to the transitions from the nonequivalent carbon sites to the lowest unoccupied, antibonding, molecular orbital.[67,68] A superposition of these features with the distinct π_1^* resonance of the phenyl rings can indeed result in the π^* resonances with the complex shapes observed for the TP1-down and TP1-up monolayers. The different relative intensities of the individual contributions within the joint π^* feature for TP1-down/Au and TP1-up/Au can be explained tentatively by the different orientations of the pyrimidine moiety with respect to the substrate. According to the literature data,[68] a substituent at either the 2 or the 5 position of pyrimidine results in different branching of the individual π^* resonances. The attachment to the substrate, even mediated by a phenyl ring and a thiolate group can provide a similar effect as a substitution at a particular site. Moreover, the highly localized core levels and the more delocalized frontier orbitals are affected to a different degree by the electrostatically induced shifts that depend on the orientation of the pyrimidine groups (see below), which can also cause deviations between the NEXAFS spectra of TP1-up and TP1-down.

The N K-edge 55° NEXAFS spectra of the TP1-down and TP1-up SAMs in Figure 4c are exclusively representative of the embedded pyrimidine moiety. They are dominated by a strong π^* resonance at 398.6 eV, accompanied by several weaker features. These spectra agree well with the spectrum of pyrimidine in the gas phase.[68] The assignments of the individual resonances can be found in a previous study.[68]

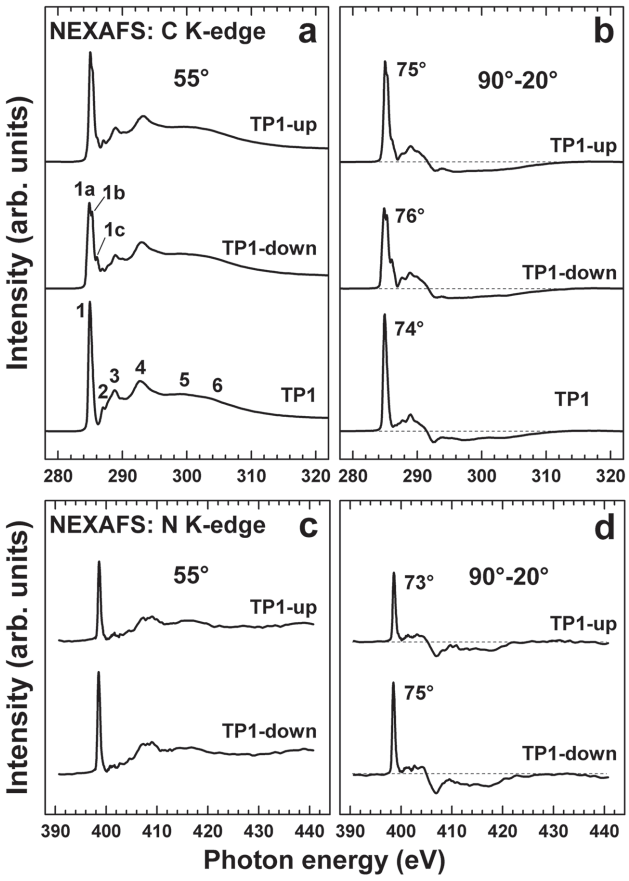

Figure 4. a,b) C and c,d) N K-edge NEXAFS spectra of the TP1, TP1-down, and TP1-up SAMs acquired at an X-ray incident angle of 55° (a,c), along with the respective difference between the spectra collected under the normal (90°) and grazing (20°) incidence geometry (b,d). Individual absorption resonances are marked by numbers (see text for the assignments). The derived average tilt angles of the π^* orbitals of the phenyl rings (C K-edge) and embedded pyrimidine moiety (N K-edge) are given at the respective resonances. The horizontal dashed lines in panels (b) and (d) correspond to zero.

Both C and N K-edge NEXAFS spectra of the TP1-down and TP1-up SAMs exhibit a pronounced linear dichroism, as seen in Figure 4b,d. This indicates a high orientational order in these films. Considering that the intensity of the π^* resonances is larger at normal than at grazing incidence (positive peaks in the difference spectra) and that the TDMs of these resonances are directed perpendicular to the phenyl and pyrimidine rings, an upright orientation of the molecular backbones in the target films can be concluded, in agreement with the XPS/HRXPS, ellipsometry, and IR data. This is supported by the numerical evaluation of the entire set of the NEXAFS spectra within the standard theoretical framework.[63] A similar procedure as for analogous aromatic SAMs was used to evaluate the dependencies of the intensity of the most prominent π^* resonances at the C and N K-edges on the incidence angle of the X-rays, fitting them to the theoretical curves for a vector-like orbital.[66,69] The only fitting parameter was the average tilt angle of the respective molecular

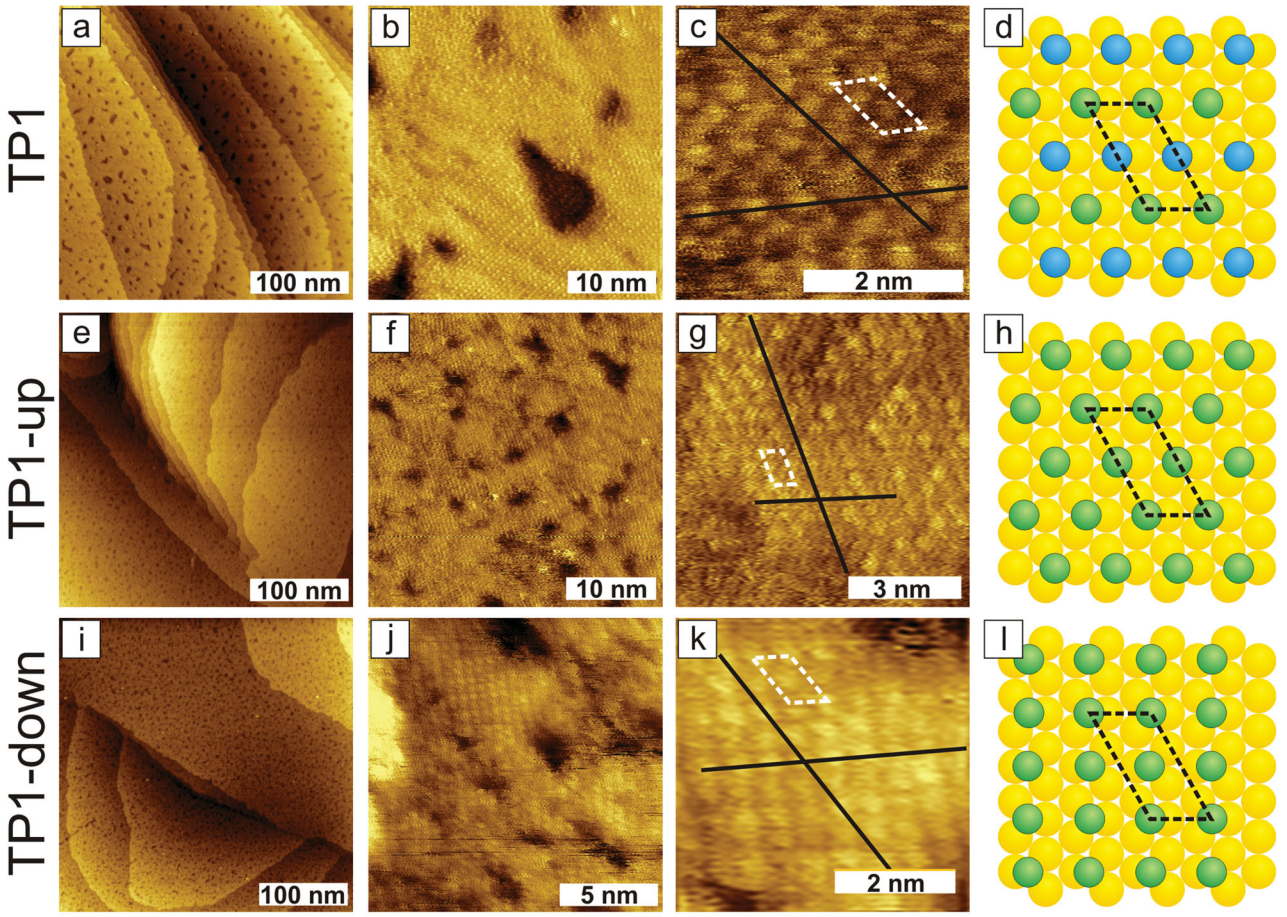

Figure 5. STM images of the a–c) TP1, e–g) TP1-down, and i–k) TP1-up SAMs taken at different magnifications, along with the tentative schematics of the respective molecular arrangements (d,h,l). The thiolate adsorption sites in the schematic structure cartoons (d,h,l) were chosen arbitrarily.

orbitals, α. The derived values of this parameter for the π^* resonances of the entire molecular backbone at the C K-edge and the π^* resonance of the pyrimidine moiety at the N K-edge are given in Figure 4b,d, at the respective absorption resonances. Significantly, the average tilt angles derived from the C and N K-edge data for both TP1-down and TP1-up SAMs are almost identical, suggesting a planar or close-to-planar molecular conformation of the aromatic backbones. Finally, based on the α values and a reasonable assumption for the twist angle, γ (32°),[57] the tilt angles of the entire molecular backbones in the target and reference SAMs, β, were calculated using the standard formula, $\cos \alpha = \sin \beta \times \cos \gamma$.[54] They are 17°, 18°, and 18° for TP1-down/Au, TP1-up/Au, and TP1/Au, respectively; the error bars can be estimated at ±3°.

2.1.5. Scanning Tunneling Microscopy

STM data for the TP1, TP1-down, and TP1-up SAMs are presented in **Figure 5**. The structure of the reference TP1 monolayer has been determined in previous studies and, thus, could be used as a benchmark.[41–43,45] In agreement with the literature data, the molecules in the TP1 SAMs were found to adopt a commensurate $(2\sqrt{3} \times \sqrt{3})R30°$ arrangement on the Au(111) terraces (Figure 5a–c) with the presence of etch pits of ≈0.24 nm depth, corresponding to a local absence of a gold monolayer. This feature is characteristic of both alkanethiolate and benzylthiolate SAMs.[70,71] The $(2\sqrt{3} \times \sqrt{3})R30°$ unit cell contains two nonequivalent molecules, which appear at slightly different heights as can be deduced from the height profiles (see Figure S5, Supporting Information). A model of this structure is shown in Figure 5d. It agrees fully with the literature data,[41–43,45] underlining the reliability of our STM experiments.

The films formed by the TP1-up molecules look very similar to TP1/Au at first sight (Figure 5e–g). In particular, many monolayer deep etch pits can be found (Figure 5e). However, these etch pits are on average smaller and more numerous than for TP1/Au, limiting the size of the ordered domains to ≈10 nm. Nevertheless, molecular resolution could be attained, revealing an approximately hexagonal pattern (Figure 5g). Height profiles (see Figure S5, Supporting Information) again suggest a $(2\sqrt{3} \times \sqrt{3})R30°$ arrangement as in case of TP1/Au. An important difference, however, is that all of the molecules in this arrangement seem to be equivalent, as indicated by using the same color code for all the adsorbates in Figure 5h. This arrangement, in principle, would also permit the assignment of the simpler $(\sqrt{3} \times \sqrt{3})R30°$ unit cell, which nevertheless does not change the associated molecular density (see below).

Molecular resolution imaging of the TP1-down SAMs turned out to be more difficult. As seen in Figure 5i,j, the etch pit appearance is similar to TP1-up/Au, again limiting the size of the crystalline areas. While the dimensions of the unit cell are basically the same as for TP1/Au and TP1-up/Au (see Figure S5, Supporting Information), the arrangement of the molecules looks somewhat different. This arrangement can be derived from the TP1-up structure by moving every other row one binding site along the ⟨11-2⟩ direction (by 0.12 nm, from a formally hcp to a fcc site or vice versa). This results in an almost square placement of the adsorbates, which, however can again be described as a centered $(2\sqrt{3} \times \sqrt{3})R30°$ structure, due to the formal nonequivalence of the adsorption sites. Note that although the adsorption sites are formally different, the appearance of the molecules in the STM images suggests similar electronic coupling to the STM tip. We have to assume that this apparent shift of the molecular rows indeed cannot occur, because it would result in impossibly small distance between the π-systems. Accordingly such a structure could not be reproduced by the theoretical calculations. We believe, rather, that we image an electronic feature at the top of the molecules, which might not be concentric with the main axis of the molecules. In any case, the packing density in the TP1-down case as well as the surface unit cell are basically the same as for TP1/Au and TP1-up/Au, in agreement with the spectroscopic data presented above.

2.2. Electrostatic Effects

2.2.1. Photoemission

The C 1s HRXP spectra of the TP1-down and TP1-up SAMs are presented in **Figure 6**, along with the data for the reference TP1 monolayer. The spectra are tentatively decomposed into several individual peaks. The curves for a PE of 350 eV can be directly compared. In accordance with literature data,[44,72] the spectrum of TP1/Au shows a strong and sharp emission at ≈284.25 eV accompanied by a weak shoulder at ≈284.95 eV assigned to the terphenyl backbone and shake-up processes in the aromatic matrix, respectively.[72] The major emission contains contributions from all carbon atoms along the molecular chain, merging in a single sharp line,[50] but its BE position is mostly representative of the ambient-adjacent phenyl ring since the photoemission signals from the central and substrate-adjacent rings are strongly attenuated at the given kinetic energy (≈60 eV at a PE of 350 eV).[35,73] In contrast, the spectra of the TP1-down and TP1-up SAMs exhibit much more complex patterns that cannot be explained by the presence of the pyrimidine ring within the standard concept of a chemical shift. Indeed, according to the reference measurements on 2-mercaptopyrimidine (2-MPM/Au, a single "pyrimidine-up" unit bearing a thiol; see Figures S6 and S7, Supporting Information) which, in terms of the branching, agree with the literature data for pyrimidine in the gas phase,[67] the spectrum of the pyrimidine moiety comprises two emissions at BEs of 285.0 and 286.4 eV having an intensity relation of 3:1. In the case of TP1-down/Au and TP1-up/Au, the respective emissions can appear at somewhat different binding energies but, most importantly, should be weak compared to the contribution from the ambient-adjacent phenyl ring. The latter is naturally associated with the prevalent peak (shaded in blue) in the 350 eV spectra of the TP1-down and TP1-up SAMs with a BE of 283.83 and 284.90 eV, respectively. This association, however, means that the emission of the ambient-adjacent ring shifts by –0.42 eV for TP1-down/Au and +0.65 eV for TP1-up/Au compared to TP1/Au. The origin of this shift cannot be chemical but only electrostatic since the only difference between the TP1-down and TP1-up molecules is the direction of the polar pyrimidine moiety. Note that a weak electron withdrawing effect, associated with the adjacent nitrogen atoms in the case of the TP1-down SAM,

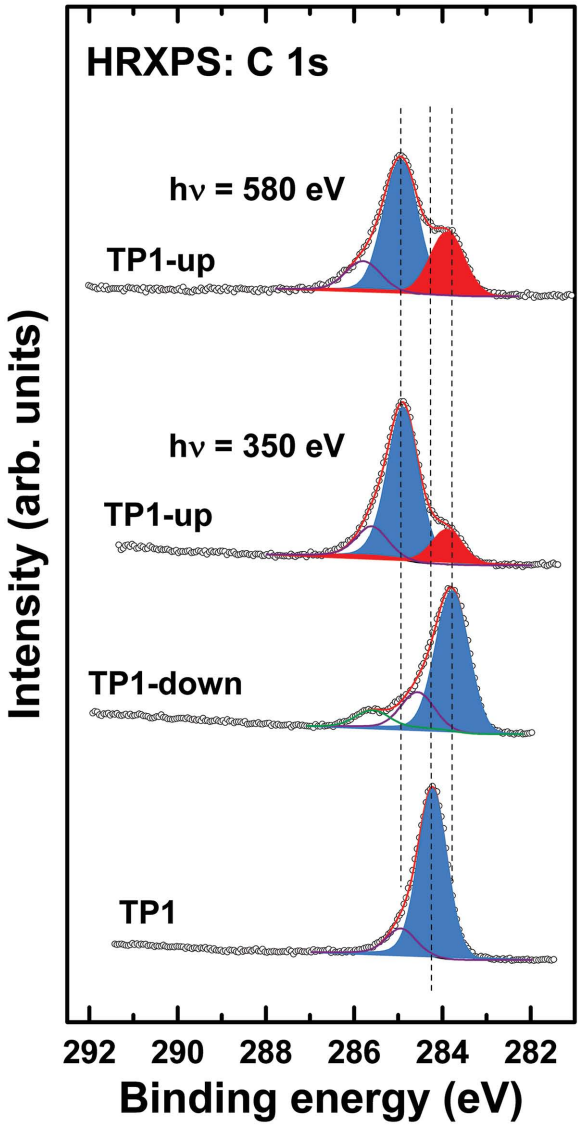

Figure 6. C 1s HRXP spectra of the TP1, TP1-down, and TP1-up SAMs acquired at photon energies of 350 and 580 eV (top spectrum; for TP1-up/Au only). The spectra are tentatively decomposed in several individual components (see text for details). The components predominantly associated with the ambient-adjacent and substrate-adjacent phenyl rings are marked by blue and red colors, respectively. The components associated with the pyrimidine ring are drawn by thin solid lines, as far as they do not overlap completely with the other features. The vertical dashed lines are guides for the eyes.

cannot produce a BE shift of such a magnitude over the entire ambient-adjacent ring.

As far as the signals originating from carbon atoms residing in the other rings are concerned, features at higher binding energies are tentatively associated with the pyrimidine and shake-up processes (vide supra). The low BE peak at 283.85 eV that is clearly resolved in the TP1-up spectrum is associated with the substrate-adjacent ring. Screening of the photoemission hole by the electrons in the metal substrate is particularly strong and relevant for the energetic position of that peak[50] resulting in a shift to lower binding energies. Conversely, the position of that peak is not subject to electrostatic shifts caused by the pyrimidines, as these reside at larger distances from the substrate (see below for a detailed discussion). This observation explains, why the 283.85 eV peak is best resolved in the TP1-up case, where the screening induced shift of the peak associated with the substrate-adjacent ring and the electrostatic shifts affecting the BE position of the dominant feature stemming from the ambient-adjacent ring go in opposite directions. In the TP1-down case, where both shifts go in the same direction, those two features overlap. The assignment that the lowest-binding energy peak originates from the carbon atoms "buried" in the monolayer is in fact supported by the spectrum shown in the top panel of Figure 6. There, the intensity of the lowest BE emission is shown to increase significantly upon increasing the kinetic energy of the photoelectrons (PE = 580 eV) due to a weaker attenuation of the respective signal.[73]

2.2.2. Work Function

Work function (WF) values for TP1/Au, TP1-down/Au, and TP1-up/Au with respect to the WF of freshly sputtered gold, measured with a Kelvin probe and derived from the secondary electron cutoffs of the ultraviolet photoemission spectra, are presented in **Figure 7** and compiled in **Table 3**, together with the theoretical values obtained from the DFT calculations (vide infra). The experimentally observed WF change upon the assembly of the TP1 monolayer compared to clean Au(111) correlates well with the literature value for the analogous molecular films, viz. −(0.8–1.0) eV.[74] Most significantly, compared to the WF of TP1/Au, TP1-down/Au, and TP1-up/Au exhibit changes of +0.55 and −0.43 eV according to the Kelvin probe, and +0.58 and −0.41 eV, according to the ultraviolet photoemission spectroscopy (UPS). This clearly manifests the electrostatic effect of the embedded dipoles.

2.2.3. Band-Structure Calculations

The main impact of the pyrimidine rings on the electronic structure of the SAM-mediated interface can be seen in **Figure 8**a, where the calculated plane-averaged electrostatic energies of TP1, TP1-up, and TP1-down SAMs on Au(111) are shown. For the substrate-adjacent phenyl ring, the electrostatic energies in the three systems coincide, while the electronic landscape experienced by the ambient-adjacent ring is shifted considerably in the TP1-up and TP1-down SAMs

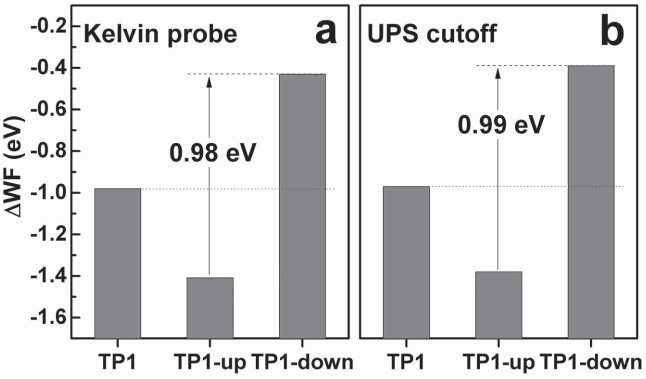

Figure 7. Work function values for TP1/Au, TP1-down/Au, and TP1-up/Au measured with a) a Kelvin probe and b) as the cutoff of the UP spectra. The values are references to the WF of freshly sputtered gold. The difference between the values for TP1-down/Au and TP1-up/Au is highlighted by arrows and precisely marked.

due to the aligned pyrimidine dipoles. This has two consequences of direct relevance for the properties discussed here: First, the vacuum level above the SAM is shifted significantly, with SAM-induced WF shifts (ΔWF) of −1.30 eV for the TP1 SAM, −0.54 eV for the TP1-down SAM, and −1.99 eV for the TP1-up SAMs, respectively. These values, summarized in Table 3, are in good semiquantitative agreement with the experimental results. More importantly, from the electrostatic energies shown in Figure 8a, one can understand why embedding the dipole in the TP1-down fashion leads to an increase of the WF compared to TP1 (the reference system containing no pyrimidine unit), while inserting it in the TP1-up orientation yields a more pronounced WF decrease. Quantitatively, the effect of reversing the orientation of the embedded pyrimidine dipole results in a WF difference between the TP1-down and TP1-up layers amounting to ΔWF^{calc} = 1.45 eV. This shift is somewhat larger than the one measured in the UPS experiments (ΔWF^{UPS} = 0.99 eV) and Kelvin probe measurements (ΔWF^{KP} = 0.98 eV). Possible reasons for this deviation are discussed in the next section.

The second immediate consequence of the shift in the electrostatic energy induced by the pyrimidine dipoles is a change in the energies of the core-levels along the backbone of the SAM constituents. The calculated energies of the C 1s states in the aromatic system relative to that of the carbon atom in the methylene linker are shown in Figure 8b. One sees that the energies of the core levels are shifted between the substrate-adjacent and ambient-adjacent rings in accordance with the shift in the potential energy shown in Figure 8a. The core-levels

Table 3. Experimental (Kelvin probe and secondary electron cutoff in UPS) and calculated (DFT) WF changes induced by the TP1, TP1-down, and TP1-up SAMs, with respect to the WF of pristine gold. The WF shifts with respect to TP1/Au are presented in parentheses. All values are given in eV.

Monolayer	Kelvin probe	UPS cutoff	DFT
TP1	−0.98	−0.97	−1.30
TP1-down	−0.43 (+0.55)	−0.39 (+0.58)	−0.54 (+0.76)
TP1-up	−1.41 (−0.43)	−1.38 (−0.41)	−1.99 (−0.69)

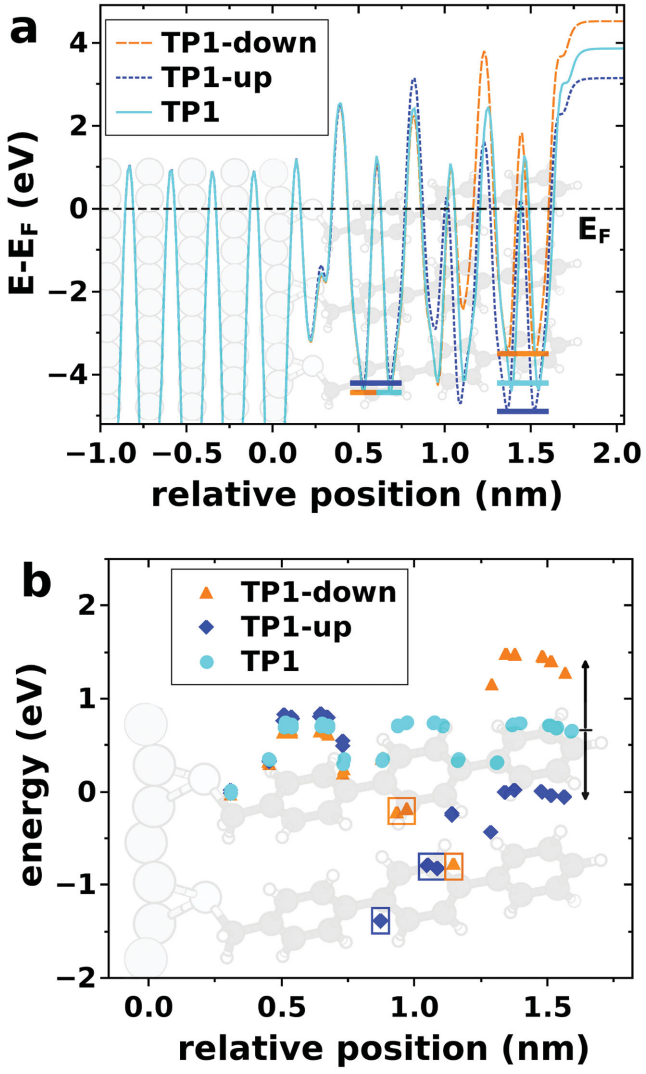

Figure 8. a) Calculated plane-averaged electrostatic energy of an electron across TP1/Au (cyan solid line), TP1-up/Au (blue dotted line), and TP1-down/Au (orange dashed line). The origin of the *x*-axis is set to the topmost metal layer while the energy scale is aligned to the Fermi energy of the substrate (see dashed horizontal line). Thick, color-coded, horizontal lines serve to illustrate the difference in electrostatic energy below and above the pyrimidine ring. b) Calculated C 1s core-level energies of TP1/Au (cyan circles), TP1-up (blue diamonds), and TP1-down/Au (orange triangles). The origin of the *x*-axis is set to the top metal layer while the energy scale is aligned to the C 1s energy of the first carbon atom in each system. Framed data points correspond to the carbon atoms bound to nitrogen and the vertical arrows indicate the difference in the core-level energies corresponding to the ambient-adjacent phenyl ring of the TP1-up and TP1-down SAMs.

of the carbon atoms bound to nitrogens are shifted to larger binding energies, which is a consequence of the changed bonding situation of those atoms (cf. data points in Figure 8b highlighted by rectangles). Consequently, these shifts can be regarded as standard "chemical shifts" while the energy differences between the carbon atoms comprising the ambient-adjacent and substrate-adjacent phenyl rings must be regarded as "electrostatic shifts."

For a quantitative comparison of the calculated core-level energies to the binding energies measured by HRXPS, in general, screening effects associated with the core–hole produced in the photoionization process also need to be considered. For signals arising from the ambient-adjacent ring, these effects are, however, comparably small keeping in mind the highly nonlinear dependence of screening on the distance from the metal surface. A first estimate of the energy correction can be obtained by means of a classical image potential,[75] using an image plane position that is located at 0.09 nm above the top row of the gold atoms.[76] This yields only comparably small and, most importantly, very similar screening-induced shifts of 0.30 eV for the lowest and 0.24 eV for the topmost C atom of the ambient-adjacent ring of the TP1 system.[77] Moreover, it needs to be kept in mind that these shifts do not affect a comparison of the features of the various SAMs that arise from C atoms at equivalent distances to the substrate. Thus, a comparison of the relative core-level shifts in the ambient-adjacent ring to the measured shifts of the dominant HRXPS feature appears sensible. The calculated upward shifts of the core-levels by +0.74 (+0.62) eV for TP1-down/Au (resulting in a reduction of the C 1s binding energies) and the downward shift by –0.73 (–0.71) eV in the TP1-up/Au case (effectively increasing the C 1s binding energies) are in good agreement with the experimental data. Note that the shifts quoted here are obtained by averaging over the core-level energies of the C atoms in the ambient-adjacent ring, while the values in parentheses are obtained, when just considering the topmost C atom of this ring.

In passing we note that as far as the intramolecular structure within the SAMs is concerned, no major differences between TP1 and TP1-up and also TP1-down are observed: In particular the inter-ring twist-angles are essentially the same in all systems and between all rings. That is, they vary between 12° and 6° with the largest values occurring in systems, where ortho-hydrogens cause some repulsion. This overall close-to-planar structure is a consequence of the significant intermolecular interactions in the densely packed layers. For example, biphenyl (as an example for oligophenylenes) displays an inter-ring twist angle of 42° in the gas phase,[56] while experimental data on terphenyl in the crystalline state indicate an interring twist of only 12°,[78] fully consistent with band-structure calculations.[79] The dominant role of intermolecular interactions for the twist angles in the SAMs considered here is supported by simulations of isolated TP1-up and TP1-down molecules, for which we find that the steric repulsion between ortho-hydrogens results in an inter-ring twist of 36°–37° between the respective rings (compared to the close-to-planar structure in the SAMs mentioned above). Conversely, parts of the molecules where the N-atoms of the pyrimidines are engaged in H-bonds with opposing ortho-hydrogens are planar.

3. Discussion

As stated in the Introduction, the major goal of this study was to realize a model SAM-mediated interface that permits control of the work function while retaining the surface chemistry and basic structural motif of the SAM-forming compounds. It was particularly important to deal with aromatic monolayers since

they possess superior transport properties and provide a good match to organic semiconductors.

As shown above, such monolayers can be successfully formed in a well-defined fashion. Significantly, the results of the complementary experimental techniques agree well with each other providing a consistent and detailed description of the systems studied.

According to the HRXPS data (Figure 2 and Table 1), all molecules in the TP1-down and TP1-up SAMs are bound to the substrate via the thiolate anchor. The monolayers are densely packed and exhibit effective thicknesses close to the molecular length of the respective precursors (≈1.5 nm), with addition of the S—Au bond length (0.24 nm).[80,81] This suggests an almost upright orientation for the TP1-down and TP1-up molecules in their respective SAMs, similar to TP1/Au.[44,45]

Indeed, both IRRAS and NEXAFS data confirm that orientation. In particular, the analysis of the IR data (Figure 3 and Table 2) yields tilt angles of 12° and 18° and twist angles of 28° and 37° for the TP1-down and TP1-up monolayers, respectively. In agreement, the evaluation of the NEXAFS data (Figure 4) results in an average tilt angle of 17°–18° for both TP1-down and TP1-up SAMs, making a reasonable assumption regarding the value of the twist angle, viz. 32°, which is characteristic of bulk terphenyl[57] and close to the average of the IR-derived angles. Significantly, the tilt angles derived from the spectra representative of the phenyl and pyrimidine rings (C and N K-edges, respectively) practically coincide (Figure 4), which suggests a planar or close-to-planar molecular conformation in both TP1-down and TP1-up monolayers, as expected for densely packed aromatic SAMs.[61] The calculated tilt angles of 13° (TP1-up) and 12° (TP1-down) also agree well to the experimental ones. In the context of this paper, it is important that these tilt angles are practically identical to that of the reference TP1 monolayer, implying that the inclusion of a pyrimidine moiety into the terphenyl backbone does not significantly change the molecular orientation in the respective SAMs. Obviously, the van der Waals and electrostatic interactions between the molecular backbones are stronger than the dipole-dipole repulsions, which would favor a significant tilt.[82,83]

Certain differences in the details of the lateral packing between the TP1-down and TP1-up SAMs do, however, occur as can be seen in the STM data (Figure 5). At the same time, the acquired data confirm high quality and dense molecular packing in the TP1-down and TP1-up monolayers. The SAMs are shown to exhibit ordered molecular lattices on the Au(111) surface that are close to the $(2\sqrt{3} \times \sqrt{3})R30°$ "parent" structure of the TP1 monolayer.[41–43,45]

This results for all three SAMs in packing densities of $\approx 4.6 \times 10^{14}$ molecules cm^{-2}, corresponding to 0.216 nm^2 per molecule. For the TP1 SAMs, these STM-derived packing densities are fully consistent with the insight gained from the XPS/HRXPS and ellipsometry data (Table 1). In the latter two experiments, a slightly reduced packing density is, however, observed for the TP1-up and TP1-down SAMs compared to the reference TP1 monolayer. In conjunction with the STM data, we attribute this to the high number of etch pits seen for the TP1-up and TP1-down SAMs, giving rise to a larger amount of domain boundaries that are potentially packed less densely. This directly affects the packing density values obtained in the XPS/HRXPS and ellipsometry experiments, which average over macroscopic sample areas. In contrast, STM typically focuses on the properties within highly ordered domains for quantitative evaluation.

The above analysis qualifies the TP1-up and TP1-down SAMs along with the reference TP1 monolayer as well-defined model systems to study the electrostatic effects of the embedded dipole in aromatic monolayer films. The most important electrostatic effect, defined as a major goal of the present study and observed here for the first time, is a WF variation induced by the embedded dipole that can be varied by changing the orientation of the pyrimidine ring. As listed in Table 3, the TP1-up and TP1-down SAMs yield WF changes of +0.55 (+0.58) and –0.43 (–0.41) eV with respect to the nonpolar TP1 monolayer, as determined by the Kelvin probe (UPS cutoff) measurements. The directions of the WF changes correlate perfectly with the orientations of the dipole moment of the embedded pyrimidine moiety, which is one more evidence that this moiety is the cause of the observed changes.

This is also fully confirmed by the DFT calculations (Figure 8a and Table 3). These simulations intrinsically consider an optimized tilt angle of the molecular dipoles as well as depolarization effects originating from the polarization of the molecular electron cloud due to the combined electrical fields of the surrounding dipoles. The latter effect has been shown to severely limit the achievable WF changes when assembling dipoles in parallel arrays.[84–86] For example, Wang et al.[87] have estimated the depolarization-induced reduction of ΔWF in $—NH_2$ tail group-substituted oligophenylene SAMs to amount to a factor of ≈3.5. In the present case, where a polarizable medium is located below and above the embedded dipoles, this effect could even be larger. Nevertheless, simulations predict sizable WF shifts of +0.76 and –0.69 eV for the TP1-down and TP1-up films, respectively. These values are somewhat larger than the experimental values in spite of similar tilt angles and packing densities. We attribute that, on the one hand, to the fact that the boundaries between the monocrystalline domains and other film imperfections caused, e.g., by etch pits cannot be accounted for in the simulations (cf., above discussion of reduced packing density of the TP1-up and TP1-down films). That this is related to the too large calculated WF shifts is supported by the observation that especially for the TP1-up SAM, where the dipoles due to the thiolate docking group and the pyrimidine point in the same direction, the absolute magnitude of ΔWF is overestimated most severely (cf., Table 3). On the other hand, certain methodological shortcomings cannot be excluded bearing in mind that (semi)local exchange-correlation functionals are known to have difficulties describing molecular dipole moments and polarizabilities accurately (a recent benchmarking study for organic molecules can be found in the literature).[88]

Another electrostatic effect of the embedded dipole is the shifts in the BE position of the C 1s emission associated with the ambient-adjacent phenyl ring in the molecular backbone (Figure 6). As mentioned in the introductory section, a similar effect has been observed for alkanethiolate SAMs with a mid-chain-embedded ester group (upward dipole direction only).[30] This, in fact, underlines the generality of this phenomenon and its independence of the backbone character. The values of these

BE shifts are –0.42 and +0.65 eV for the TP1-down and TP1-up SAMs compared to the reference TP1 film, while the calculated BE shifts amount to –0.74 and +0.73 eV, when averaging over all C atoms in the ambient-adjacent ring, and –0.62 and +0.71 eV, when considering only the topmost C atom (cf., Figure 8b; note that a downward shift of the energy of a core level results in an increase of the binding energy and vice versa). Again, the direction of the shift correlates perfectly with the direction of the embedded dipole. As mentioned above, the occurrence of this shift (along with the electrostatic effects observed in XP spectra of several different SAM systems)[31–34] cannot be explained solely on the basis of chemical shifts, where the only origin for differences in the binding energies is assumed to lie in the local chemical environment of an atom. This applies perfectly to conductive samples connected electrically to the spectrometer, where no electric fields (and, thus, local potential energy gradients) can occur. In dielectric samples, the situation is fundamentally different: There, for example, aligned dipole layers can induce a shift of the electrostatic energy between different regions of the sample as illustrated in Figure 8a. This change in the local energy results in a concomitant local shift of the positions of the core levels (see Figure 8b). Accordingly, a decrease in the electrostatic energy results in a shift of the photoemission line to higher binding energies, with the opposite being true for an increase in the electrostatic energy. This is exactly what we observe in the C 1s HRXP spectra of the TP1-down and TP1-up SAMs in Figure 6. In that sense, XPS core levels act as an efficient probe of the local electrostatic environments of a particular chemical species. The electrostatic shifts are superimposed with "traditional" chemical shift associated in our case with the nitrogen atoms of the pyrimidine ring. Interestingly, in the present case, the shift in the photoemission peaks associated with the ambient-adjacent ring correlates well with the WF changes induced by the pyrimidine-containing SAMs (compared to the TP1 SAM as a reference). In view of the model described above, this observation can be rationalized by the fact that both the shifts of the photoemission peaks as well as the respective relative WF changes are caused by the parallel arrangement of the pyrimidine dipoles and the resulting modification of the potential-energy landscape.

The fact that the embedded dipoles work so well is related to two additional effects that have not been mentioned so far: First, these potential energy shifts occur quite abruptly, which is an electrostatic peculiarity: Natan et al.[89] have shown that the decay length of the electric field caused by an arrangement of point dipoles is nearly an order of magnitude shorter than the inter-dipole distance. Second, the charge transfer between the substrate and the core hole is a comparably slow process on the timescale of the photoemission both in aliphatic[90] and aromatic[91] SAMs. Especially, when considering photoionization of the carbon atoms in the ambient-adjacent ring it is reasonable to assume that the filling of the core–hole will happen at even longer timescales. Thus, the primary source of screening is polarization of the conducting substrate (see above). Metal-to-molecule charge transfer processes are not expected to affect the measured XPS binding energies. Consequently, the electrostatic shift of the energetic positions of the C 1s orbitals, that can be inferred from the calculated potential energy distributions, directly maps onto shifts of the measured binding energies.

4. Conclusion

Using a variety of complementary experimental characterization techniques supported by DFT calculations, we investigated in detail a model system of self-assembled monolayers on gold comprising aromatic thiolates with embedded dipoles. The dipoles were introduced to the SAM precursor molecules, TP1 (terphenyl-4-methanethiol), by substituting the central phenyl ring by a 2,5-pyrimidine moiety. Altering the orientation of the pyrimidine moiety allows the realization of monolayers in which the dipole moments either point away from (TP1-up/Au) or toward the substrate (TP1-down/Au).

The results of the spectroscopic and microscopic techniques imply that the molecular orientation and the structure of the substituted monolayers closely resemble those of the nonpolar benchmark system, TP1/Au. Characterization of the electronic properties of these SAMs reveals that the embedded dipoles significantly shift the substrate work function in a systematic manner: a dipole moment pointing toward the Au substrate increases the WF, while a dipole moment pointing away decreases the WF compared to the TP1/Au benchmark system. The accessible WF range spans ≈1 V, while at the same time maintaining the chemical identity and structural properties of the SAM-ambient interface.

This implies that the strategy of embedded dipoles in interfacial, monomolecular layers opens up the possibility to decouple control over charge injection from control over the nucleation and growth of organic semiconductor layers. Thus, such films have high potential in organic electronics, where they can be used for interface engineering. Also in molecular electronics they allow the study of electrostatic effects independently of the (top) contact properties.

Specific electrostatic properties of such systems go beyond work function control, leading, in particular, to interesting effects in photoemission, calling into question the commonly applied concept that chemical shifts are the only cause for shifts in core-level binding energies.

Finally, the observation that dipole-induced electrostatic shifts within monolayers can be realized and efficiently characterized experimentally raises the question, whether also considerably more complex, electrostatically designed structures will become available as "real-world" systems already in the near future. Such structures can comprise, for example, monolayer quantum wells and quantum cascades realized by a deliberate combination of dipolar and semiconducting elements within one molecule, as suggested recently on the basis of quantum-mechanical simulations.[92]

5. Experimental Section

Compounds and Chemicals: While the synthesis of TP1 has been described in the literature and was performed accordingly,[42,93] the procedure for the pyrimidine containing molecules, TP1-up and TP1-down, had to be developed. The strategy to synthesize these molecules is

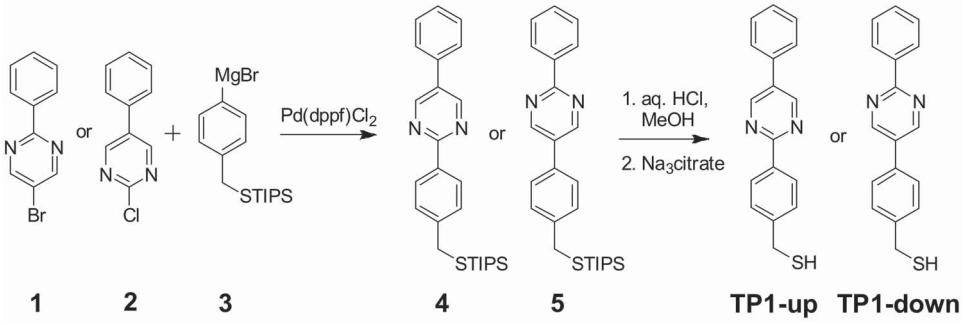

Scheme 1. Outline of the syntheses of the dipolar molecules, TP1-up and TP1-down. The Grignard reagent **3** already bears the thiol group in a protected form, simplifying the synthetic strategy.

summarized in **Scheme 1**. The Kumada coupling of the Grignard reagent **3**, formed from 4-bromobenzyl(triisopropylsilyl)sulfide, with amino- or pyridine-terminated bromophenyl-derivatives has been developed and optimized previously.[94] The synthesis of the coupling partners, 5-bromo-2-phenylpyrimidine (**1**) and 2-chloro-5-phenylpyrimidine (**2**), via Suzuki coupling reactions has been described in the literature.[95,96] The resulting triisopropylsilyl (TIPS) protected compounds **4** and **5** were deprotected protolytically using aqueous HCl in methanol. The final TP1-up and TP1-down substances are air stable as crystalline compounds but become easily oxidized to the less soluble disulfides in solution. All other chemicals, including 2-MPM, 1-dodecanethiol (DDT), and 1-hexadecanethiol (HDT) were purchased from Sigma-Aldrich and used as received.

Preparation of the SAMs: The gold substrates were purchased from Georg Albert PVD-Beschichtungen and used as received. They were prepared by thermal evaporation of 100–200 nm of gold (99.99% purity) onto polished single-crystal Si(100) wafers (Silicon Sense) primed with a 5 nm adhesion layer of titanium or chromium. The resulting metal substrates were polycrystalline, with predominant (111) orientation and a grain or terrace size of 20–50 nm as observed by atomic force microscopy and STM. For the STM studies of the SAMs (see below), 200 nm Au films on mica were purchased from Phasis (Geneva). The SAMs were formed by immersion of the substrates into solutions of the SAM precursors in ethanol (concentration range 10×10^{-6}–1000×10^{-6} M) under nitrogen at ambient temperature for 24 h. After immersion, the samples were carefully rinsed with pure solvent and blown dry with a stream of N_2 or Ar. In addition to the target TP1-up and TP1-down films, we also prepared reference SAMs of TP1 and 2-MPM. We also prepared alkanethiolate monolayers, viz. those of DDT and HDT, as references for the measurement of the effective thicknesses and packing densities, applying the standard preparation procedure.[2]

Characterization of the SAMs: General Comments: The target and reference SAMs were characterized by XPS, HRXPS, ellipsometry, NEXAFS spectroscopy, IRRAS, and STM. All experiments were performed at room temperature. The XPS, HRXPS, and NEXAFS spectroscopy measurements were conducted under ultra-high vacuum (UHV) conditions at a base pressure better than 1.5×10^{-9} mbar. Special care was taken to minimize and avoid damage to the samples induced by X-rays during the measurements.[50,97]

Ellipsometry: Ellipsometry measurements on the SAMs were conducted with a Sentech SE 400 ellipsometer equipped with a He/Ne laser (wavelength 632.8 nm, beam diameter 1–2 mm). The angle of incidence was 70° with respect to the sample surface normal. The complex refractive indices of the substrates, necessary for the data evaluation, were measured separately after a hydrogen plasma treatment for 2 min.[98] For the refractive indices of the monolayers, the extinction coefficients were assumed to be zero, while the real part was assumed to be 1.55, a value that from our experience is well applicable in the case of mainly aromatic molecules.

XPS and HRXPS: The XPS measurements were performed using a laboratory spectrometer equipped with a Mg Kα X-ray source and an LHS11 analyzer. The spectra acquisition was carried out in normal emission geometry with an energy resolution of ≈0.9 eV. The X-ray source was operated at 260 W power and positioned ≈1 cm away from the samples. The BE scale was referenced to the Au $4f_{7/2}$ peak at a BE of 84.0 eV.[99] Since the quality of the XP spectra was inferior to the HRXPS data, they only were used to determine the effective thickness and packing density in the TP1, TP1-up, and TP1-down monolayers. HRXPS measurements were conducted at the bending magnet beamline D1011 of the MAX-IV synchrotron radiation facility in Lund, Sweden, using a SCIENTA SES200 electron energy analyzer. The spectra were recorded in the Au 4f, S 2p, C 1s, N 1s, and O 1s regions. The spectra acquisition was performed in normal emission geometry and at PEs ranging from 350 to 580 eV. The BE scale of every spectrum was individually calibrated to the Au $4f_{7/2}$ emission of the gold substrate at 84.0 eV.[99] The energy resolution was better than 100 meV (mostly around 70 meV), which is noticeably smaller than the full width at half maximum (fwhm) of the spectral features relevant in this study. Both XP and HRXP spectra were fitted by symmetric Voigt functions and either Shirley-type or linear backgrounds. To fit the S $2p_{3/2,1/2}$ doublet, we used two peaks with the same fwhm, the standard[99] spin–orbit splitting of ≈1.18 eV (verified by fit), and a branching ratio of 2 (S $2p_{3/2}$/S $2p_{1/2}$). For all samples, the same fit parameters were used for identical spectral regions for a given photon energy. The effective film thicknesses were calculated by evaluating the intensity ratios of the C 1s and Au 4f emissions,[100] and using a DDT SAM—a film of well-defined thickness (1.5 nm)[101]—as a reference system. A standard, exponential attenuation of the photoemission signal was assumed; attenuation lengths determined for a series of nonsubstituted alkanethiolate SAMs were used.[102] Further, the packing densities were coarsely estimated from the intensity ratios of the S 2p and Au 4f emissions, following the approach of refs. [103] and [104]. As reference systems of reproducible quality and with well-known packing density (0.216 nm^2 molecule^{-1}; 4.63×10^{14} molecules cm^{-2})[105,106] DDT and HDT SAMs on Au(111) were used.

NEXAFS Spectroscopy: NEXAFS spectroscopy experiments were performed at the same beamline as the HRXPS measurements. The spectra were acquired at the carbon and nitrogen K-edges in the partial electron yield acquisition mode with retarding voltages of −150 and −300 V, respectively. Linear-polarized synchrotron light with a polarization factor of ≈95% was used. The energy resolution was better than 100 meV at the C K-edge and ≈100 meV at the N K-edge. The incidence angle of the X-rays was varied from 90° (**E** vector in surface plane) to 20° (**E** vector nearly parallel to surface normal) in steps of 10°–20° to monitor the orientational order in the SAMs. This approach is based on the linear dichroism in X-ray absorption, i.e., the dependence of the cross-section of the resonant photoexcitation process on the orientation of the electric field vector of the synchrotron light with respect to the molecular orbital of interest.[63] Raw NEXAFS spectra were normalized to the incident photon flux determined from the spectrum of a clean, freshly sputtered gold sample. Subsequently, they were reduced to the standard form by subtracting a linear preedge background and by normalizing to the unity edge jump. The energy scale was calibrated

by means of the most intense π^* resonance of highly oriented pyrolytic graphite (HOPG) at 285.38 eV[107] in combination with the well-known $\Delta h\nu \propto (h\nu)^{3/2}$ behavior of plane grating monochromators.[108]

Infrared Spectroscopy: IR spectra of the precursor substances and SAMs were recorded using a Thermo Nicolet 6700 Fourier transform IR spectrometer with a liquid nitrogen-cooled narrow band cadmium telluride semiconductor detector. During registration of the spectra, the beam path of the spectrometer was purged with dried and CO_2-free air. All spectra were acquired at a resolution of 4 cm^{-1}. Neat substance spectra were obtained using a single-reflection diamond attenuated total reflection unit. Spectra of the SAMs were measured with an infrared reflection–absorption unit using *p*-polarized IR radiation at an incidence angle of 80° relative to the sample surface normal. Perdeuterated DDT SAMs on gold served as reference for the IRRAS measurements. For each SAM, at least 2000 scans were averaged, followed by a smooth baseline correction. DFT calculations of the isolated molecules were performed with the Gaussian09 program package[109] at the BP86[110,111]/SVP[112] level to aid the band assignment in the experimental spectra and to obtain the directions of the TDMs of the most pronounced vibrational modes.

Scanning Tunneling Microscopy: For the STM experiments, a Bruker MultiMode 8 SPM Nanoscope with a MultiMode V SPM Control Station was employed. Measurements in the sub-nA regime were carried out with a Low Current STM Converter (Model MMSTMLCE). A typical measurement current was around 5 pA at a sample bias of about 200 mV. The scanner head had a maximum range of 1400 nm × 1400 nm. As probes, Pt-Ir (80:20) wires with a diameter of 0.25 mm were hand cut and the tip quality assessed by measuring a HOPG sample. Only monolayers on gold deposited onto mica were used to ensure the presence of flat terraces.

Determination of the Work Function: Two alternative methods were used. First, the WF was determined by measuring the secondary electron cutoff of the UP spectra following a standard approach.[31] The experiments were performed at the Max IV facility, using the same beamline and experimental station as in the case of the HRXPS and NEXAFS measurements. The photon energy was set to 50 eV. UPS was performed by biasing the samples −25.6 V relative to ground so that the low energy portion of the spectrum could be observed. The positions of the cutoff in the target samples were referenced to those of HDT/Au and freshly sputtered gold. Second, WF measurements were carried out using a UHV Kelvin Probe 2001 system (KP technology Ltd., UK). The pressure in the UHV chamber was ≈10^{-10} mbar. The positions of the cutoff in the target samples were referenced to those of HDT/Au and freshly sputtered gold.

Band-Structure Calculations: We modeled the substrate-SAM interfaces using a ($\sqrt{3} \times 3$) surface unit cell containing two molecules. This structure is equivalent to the ($2\sqrt{3} \times \sqrt{3}$)R30° arrangement reported in the literature for TP1 monolayers on gold[41–43,45] and also close to the 2D lattice of the TP1-up and TP1-down SAMs obtained in the present study (see discussion of the STM data). A herringbone arrangement was assumed for the molecules and the substrate was represented by five layers of Au. Along the surface normal, we inserted a vacuum gap of ≈2.0 nm and applied a dipole correction to adapt the internal 3D-periodicity of the band-structure calculations to the periodicity of our system (extended 2D-periodic surfaces). DFT based band-structure calculations using the plane-wave code VASP[113] were performed. We employed convergence criteria of 10^{-4} eV for the total energy in the electronic self-consistent cycle and 10^{-1} eV nm^{-1} for optimizing the forces in ionic relaxations. Additionally, we checked the convergence of the dipole moment per unit cell to ensure that the calculated WF changes are converged to within 10^{-2} eV. The geometry optimizations were performed using the GADGET tool, which allowed for the use of internal coordinates in the optimizations.[114] A (8 × 5 × 1) Monkhorst-Pack[115] *k*-point grid was chosen to represent the systems in reciprocal space (further increasing the total number of k-points by 50% resulted in differences in the WF < 0.05 eV). Core-valence interactions were described within the projected-augmented wave (PAW) formalism[116] (kinetic-energy cutoff: ≈20 Ryd; increasing the plane-wave cutoff to ≈22 Ryd changed the WF by less than 0.02 eV) and exchange correlation was treated using the Perdew–Burke–Enzerhof (PBE) functional.[117] Structural representations of the systems were generated with XCrySDen.[118] Core-level energies were computed within the so-called initial-state approximation,[119] where the Kohn–Sham energies of the core levels are computed within the PAW sphere after self-consistency was achieved.[119] Such calculations do not treat final-state effects (i.e., the impact of screening of the core hole),[119] but considering the large distance between the metal substrate and the carbon atoms relevant for the following discussion, we expect their impact to be weak (cf., above discussion of calculated core-level shifts). Simulations on isolated molecules were performed with the QChem code[120] using the PBE functional and cc-PVTZ basis functions.[121]

Supporting Information

Supporting Information is available from the Wiley Online Library or from the author.

Acknowledgements

The authors thank the Max-IV staff, and A. Preobrajenski in particular, for the technical support during the synchrotron-based experiments. This work was supported by the German Research Society (grant ZH 63/17-1) and the Austrian Science Fund (FWF): I937-N19 within the ERA-Chemistry framework and by funding from the European Community's Seventh Framework Programme (FP7/2007-2013) CALIPSO under Grant Agreement No. 312284. The computational studies presented have been performed using the clusters of the division for high-performance computing at Graz University of Technology. The authors thank the AlzChem AG, Trostberg, and Umicore AG & Co. KG, Hanau, for generous gifts of 2-hydroxypyrimidine and gold, respectively.

Received: March 6, 2015
Revised: April 27, 2015
Published online: May 22, 2015

[1] A. Ulman, *An Introduction to Ultrathin Organic Films*. From Langmuir-Blodgett to Self-Assembly, Academic, New York **1991**.
[2] J. C. Love, L. A. Estroff, J. K. Kriebel, R. G. Nuzzo, G. M. Whitesides, *Chem. Rev.* **2005**, *105*, 1103.
[3] R. G. Nuzzo, D. L. Allara, *J. Am. Chem. Soc.* **1983**, *105*, 4481.
[4] X. Feng, L. Jiang, *Adv. Mater.* **2006**, *18*, 3063.
[5] S. L. Gras, T. Mahmud, G. Rosengarten, A. Mitchell, K. Kalantar-Zadeh, *Chem. Phys. Chem.* **2007**, *8*, 2036.
[6] P. M. Mendes, *Chem. Soc. Rev.* **2008**, *37*, 2512.
[7] A. Rosenhahn, S. Schilp, H. J. Kreuzer, M. Grunze, *Phys. Chem. Chem. Phys.* **2010**, *12*, 4275.
[8] L. Srisombat, A. C. Jamison, T. R. Lee, *Colloids Surf. A* **2011**, *390*, 1.
[9] J. Landoulsi, K. E. Cooksey, V. Dupres, *Biofouling* **2011**, *27*, 1105.
[10] M. Halik, H. Klauk, U. Zschieschang, G. Schmid, C. Dehm, M. Schutz, S. Maisch, F. Effenberger, M. Brunnbauer, F. Stellacci, *Nature* **2004**, *431*, 963.
[11] H. Klauk, U. Zschieschang, J. Pflaum, M. Halik, *Nature* **2007**, *445*, 745.
[12] M. Salinas, C. M. Jäger, A. Y. Amin, P. O. Dral, T. Meyer-Friedrichsen, A. Hirsch, T. Clark, M. Halik, *J. Am. Chem. Soc.* **2012**, *134*, 12648.
[13] M. Burkhardt, A. Jedaa, M. Novak, A. Ebel, K. Voitchovsky, F. Stellacci, A. Hirsch, M. Halik, *Adv. Mater.* **2010**, *22*, 2525.
[14] P. Pacher, A. Lex, V. Proschek, H. Etschmaier, E. Tchernychova, M. Sezen, U. Scherf, W. Grogger, G. Trimmel, C. Slugovc, E. Zojer, *Adv. Mater.* **2008**, *20*, 3143.

[15] E. C. P. Smits, S. G. J. Mathijssen, P. A. van Hal, S. Setayesh, T. C. T. Geuns, K. A. H. A. Mutsaers, E. Cantatore, H. J. Wondergem, O. Werzer, R. Resel, M. Kemerink, S. Kirchmeyer, A. M. Muzafarov, S. A. Ponomarenko, B. de Boer, P. W. M. Blom, D. M. de Leeuw, *Nature* **2008**, *455*, 956.
[16] I. H. Campbell, S. Rubin, T. A. Zawodzinski, J. D. Kress, R. L. Martin, D. L. Smith, N. N. Barashkov, J. P. Ferraris, *Phys. Rev. B* **1996**, *54*, 14321.
[17] I. H. Campbell, J. D. Kress, R. L. Martin, D. L. Smith, N. N. Barashkov, J. P. Ferraris, *Appl. Phys. Lett.* **1997**, *71*, 3528.
[18] B. De Boer, A. Hadipour, M. M. Mandoc, T. van Woudenbergh, P. W. M. Blom, *Adv. Mater.* **2005**, *17*, 621.
[19] C. Bock, D. V. Pham, U. Kunze, D. Käfer, G. Witte, C. Wöll, *J. Appl. Phys.* **2006**, *100*, 114517.
[20] N. Crivillers, S. Osella, C. Van Dyck, G. M. Lazzerini, D. Cornil, A. Liscio, F. Di Stasio, S. Mian, O. Fenwick, F. Reinders, M. Neuburger, E. Treossi, M. Mayor, V. Palermo, F. Cacialli, J. Cornil, P. Samorì, *Adv. Mater.* **2013**, *25*, 432.
[21] I. Lange, S. Reiter, M. Pätzel, A. Zykov, A. Nefedov, J. Hildebrandt, S. Hecht, S. Kowarik, C. Wöll, G. Heimel, D. Neher, *Adv. Funct. Mater.* **2014**, *24*, 7014.
[22] J. Kim, Y. S. Rim, Y. Liu, A. C. Serino, J. C. Thomas, H. Chen, Y. Yang, P. S. Weiss, *Nano Lett.* **2014**, *14*, 2946.
[23] E. Margapoti, J. Li, Ö. Ceylan, M. Seifert, F. Nisic, T. Le Anh, F. Meggendorfer, C. Dragonetti, C.-A. Palma, J. V. Barth, J. J. Finley, *Adv. Mater.* **2015**, *27*, 1426.
[24] B. H. Hamadani, D. A. Corley, J. W. Ciszek, J. M. Tour, D. Natelson, *Nano Lett.* **2006**, *6*, 1303.
[25] G. Heimel, L. Romaner, J. L. Brédas, E. Zojer, *Phys. Rev. Lett.* **2006**, *96*, 196806.
[26] K. Heister, S. Frey, A. Ulman, M. Grunze, M. Zharnikov, *Langmuir* **2004**, *20*, 1222.
[27] R. M. Petoral, K. Uvdal, *J. Phys. Chem. B* **2005**, *109*, 16040.
[28] S. Krakert, N. Ballav, M. Zharnikov, A. Terfort, *Phys. Chem. Chem. Phys.* **2010**, *12*, 507.
[29] P. A. Lewis, C. E. Inman, F. Maya, J. M. Tour, J. E. Hutchison, P. S. Weiss, *J. Am. Chem. Soc.* **2005**, *127*, 17421.
[30] O. M. Cabarcos, A. Shaporenko, T. Weidner, S. Uppili, L. S. Dake, M. Zharnikov, D. L. Allara, *J. Phys. Chem. C* **2008**, *112*, 10842.
[31] H. Ahn, M. Zharnikov, J. E. Whitten, *Chem. Phys. Lett.* **2006**, *428*, 283.
[32] Y. Ge, T. Weidner, H. Ahn, J. E. Whitten, M. Zharnikov, *J. Phys. Chem. C* **2009**, *113*, 4575.
[33] N. Ballav, A. Terfort, M. Zharnikov, *J. Phys. Chem. C* **2009**, *113*, 3697.
[34] N. V. Venkataraman, S. Zuercher, A. Rossi, S. Lee, N. Naujoks, N. D. Spencer, *J. Phys. Chem. C* **2009**, *113*, 5620.
[35] B. D. Ratner, D. G. Castner, in *Surface Analysis - The Principle Techniques* (Ed: J. C. Vickerman), Wiley & Sons, Chichester **1997**.
[36] D. A. Egger, F. Rissner, G. M. Rangger, O. T. Hofmann, L. Wittwer, G. Heimel, E. Zojer, *Phys. Chem. Chem. Phys.* **2010**, *12*, 4291.
[37] N. J. Tao, *Nat. Nanotechnol.* **2006**, *1*, 173.
[38] S. Karthäuser, *J. Phys.: Condens. Matter* **2011**, *23*, 013001.
[39] C. Querebillo, A. Terfort, D. A. Allara, M. Zharnikov, *J. Phys. Chem. C* **2013**, *117*, 25556.
[40] C. Bock, D. V. Pham, U. Kunze, D. Käfer, G. Witte, A. Terfort, *Appl. Phys. Lett.* **2007**, *91*, 052110.
[41] T. Ishida, W. Mizutani, U. Akiba, K. Umemura, A. Inoue, N. Choi, M. Fujihira, H. Tokumoto, *J. Phys. Chem. B* **1999**, *103*, 1686.
[42] T. Ishida, W. Mizutani, N. Choi, U. Akiba, M. Fujihira, H. Tokumoto, *J. Phys. Chem. B* **2000**, *104*, 11680.
[43] C. Fuxen, W. Azzam, R. Arnold, G. Witte, A. Terfort, C. Wöll, *Langmuir* **2001**, *17*, 3689.
[44] A. Shaporenko, M. Brunnbauer, A. Terfort, M. Grunze, M. Zharnikov, *J. Phys. Chem. B* **2004**, *108*, 14462.
[45] W. Azzam, A. Bashir, A. Terfort, T. Strunskus, C. Woll, *Langmuir* **2006**, *22*, 3647.
[46] H. Weiler-Feilchenfeld, E. D. Bergmann, *Isr. J. Chem.* **1968**, *6*, 823.
[47] G. L. Blackman, R. D. Brown, F. R. Burden, *J. Mol. Spectrosc.* **1970**, *35*, 444.
[48] P. E. Laibinis, G. M. Whitesides, D. L. Allara, Y. T. Tao, A. N. Parikh, R. G. Nuzzo, *J. Am. Chem. Soc.* **1991**, *113*, 7152.
[49] M. Zharnikov, M. Grunze, *J. Phys.: Condens. Matter* **2001**, *13*, 11333.
[50] M. Zharnikov, *J. Electron. Spectrosc. Relat. Phenom.* **2010**, *178*, 380.
[51] R. G. Greenler, *J. Chem. Phys.* **1966**, *44*, 310.
[52] A. Parikh, D. Allara, *J. Chem. Phys.* **1992**, *96*, 927.
[53] R. Arnold, A. Terfort, C. Wöll, *Langmuir* **2001**, *17*, 4980.
[54] N. Ballav, B. Schüpbach, O. Dethloff, P. Feulner, A. Terfort, M. Zharnikov, *J. Am. Chem. Soc.* **2007**, *129*, 15416.
[55] O. Bastiansen, *Acta Chem. Scand.* **1949**, *3*, 408.
[56] A. Almenningen, O. Bastiansen, L. Fernholt, B. Cyvin, S. Cyvin, S. Samdal, *J. Mol. Struct.* **1985**, *128*, 59.
[57] H. M. Rietvield, E. N. Maslen, C. J. B. Clews, *Acta Cryst.* **1970**, *B26*, 693.
[58] J. L. Baudour, Y. Delugeard, H. Cailleau, *Acta Cryst.* **1976**, *B32*, 150.
[59] H. Cailleau, J. Baudour, J. Meinnel, A. Dworkin, F. Moussa, C. Zeyen, *Faraday Discuss.* **1980**, *69*, 7.
[60] P. Bordat, R. A Brown, *Chem. Phys.* **1999**, *246*, 323.
[61] A. Shaporenko, M. Elbing, A. Baszczyk, C. von Hanisch, M. Mayor, M. Zharnikov, *J. Phys. Chem. B* **2006**, *110*, 4307.
[62] J. Liu, B. Schüpbach, A. Bashir, O. Shekhah, A. Nefedov, M. Kind, A. Terfort, C. Wöll, *Phys. Chem. Chem. Phys.* **2010**, *12*, 4459.
[63] J. Stöhr, *NEXAFS Spectroscopy*, Springer-Verlag, Berlin **1992**.
[64] J. Horsley, J. Stöhr, A. P. Hitchcock, D. C. Newbury, A. L. Johnson, F. Sette, *J. Chem. Phys.* **1985**, *83*, 6099.
[65] T. Yokoyama, K. Seki, I. Morisada, K. Edamatsu, T. Ohta, *Phys. Scr.* **1990**, *41*, 189.
[66] S. Frey, V. Stadler, K. Heister, W. Eck, M. Zharnikov, M. Grunze, B. Zeysing, A. Terfort, *Langmuir* **2001**, *17*, 2408.
[67] P. Bolognesi, P. O'Keeffe, V. Feyer, O. Plekan, K. Prince, M. Coreno, G. Mattioli, A. A. Bonapasta, W. Zhang, V. Carravetta, Y. Ovcharenko, L. Avaldi, *J. Phys.: Conf. Ser.* **2010**, *212*, 012002.
[68] P. Bolognesi, P. O'Keeffe, Y. Ovcharenko, M. Coreno, L. Avaldi, V. Feyer, O. Plekan, K. C. Prince, W. Zhang, V. Carravetta, *J. Chem. Phys.* **2010**, *133*, 034302.
[69] M. Zharnikov, A. Kuller, A. Shaporenko, E. Schmidt, W. Eck, *Langmuir* **2003**, *19*, 4682.
[70] G. E. Poirier, *Chem. Rev.* **1997**, *97*, 1117.
[71] G. E. Poirier, *Langmuir* **1997**, *13*, 2019.
[72] A. Shaporenko, M. Brunnbauer, A. Terfort, L. S. O. Johansson, M. Grunze, M. Zharnikov, *Langmuir* **2005**, *21*, 4370.
[73] D. Briggs, M. P. Seah, *Practical Surface Analysis by Auger and X-Ray Photoelectron Spectroscopy*, 2nd ed., John Wiley, Chichester **1990**.
[74] L. Kong, F. Chesneau, Z. Zhang, F. Staier, A. Terfort, P. A. Dowben, M. Zharnikov, *J. Phys. Chem. C* **2011**, *115*, 22422.
[75] J. B. Neaton, M. S. Hybertsen, S. G. Louie, *Phys. Rev. Lett.* **2006**, *97*, 216405.
[76] D. A. Egger, Z. Liu, J. B. Neaton, L. Kronik, *Nano. Lett.* **2015**, *15*, 2448.
[77] These numbers change to 0.10 V and 0.08 eV when using a scalar dielectric constant of 3 for the SAM instead of only using the vacuum permittivity.
[78] P. J. L. Baudour, H. Cailleau, W. B. Yelon, *Acta Crystallogr. B* **1977**, *33*, 1773.
[79] P. Puschnig, C. Ambrosch-Draxl, G. Heimel, E. Zojer, R. Resel, G. Leising, M. Kriechbaum, W. Graupner, *Synth. Met.* **2001**, *116*, 327.

[80] H. Kondoh, M. Iwasaki, T. Shimada, K. Amemiya, T. Yokoyama, T. Ohta, M. Shimomura, S. Kono, *Phys. Rev. Lett.* **2003**, *90*, 066102.
[81] M. G. Roper, M. P. Skegg, C. J. Fisher, J. J. Lee, V. R. Dhanak, D. P. Woodruff, R. G. Jones, *Chem. Phys. Lett.* **2004**, *389*, 87.
[82] J. Hautman, J. P. Bareman, W. Mar, M. L. Klein, *J. Chem. Soc., Faraday Trans.* **1991**, *87*, 2031.
[83] S. Frey, A. Shaporenko, M. Zharnikov, P. Harder, D. L. Allara, *J. Phys. Chem. B* **2003**, *107*, 7716.
[84] A. Natan, Y. Zidon, Y. Shapira, L. Kronik, *Phys. Rev. B* **2006**, *73*, 193310.
[85] D. Cornil, Y. Olivier, V. Geskin, J. Cornil, *Adv. Funct. Mater.* **2007**, *17*, 1143.
[86] M. L. Sushko, A. L. Shluger, *Adv. Funct. Mater.* **2008**, *18*, 2228.
[87] L. Wang, G. M. Rangger, L. Romaner, G. Heimel, T. Bučko, Z. Ma, Q. Li, Z. Shuai, E. Zojer, *Adv. Funct. Mater.* **2009**, *19*, 3766.
[88] A. L. Hickey, C. N. Rowley, *J. Phys. Chem. A* **2014**, *118*, 3678.
[89] A. Natan, L. Kronik, H. Haick, R. T. Tung, *Adv. Mater.* **2007**, *19*, 4103.
[90] P. Kao, S. Neppl, P. Feulner, D. L. Allara, M. Zharnikov, *J. Phys. Chem. C* **2010**, *114*, 13766.
[91] H. Hamoudi, S. Neppl, P. Kao, B. Schüpbach, P. Feulner, A. Terfort, D. Allara, M. Zharnikov, *Phys. Rev. Lett.* **2011**, *107*, 027801.
[92] B. Kretz, D. A. Egger, E. A. Zojer, *Adv. Sci.* **2015**, *2*, 1400016.
[93] H. J. Himmel, A. Terfort, C. Wöll, *J. Am. Chem. Soc.* **1998**, *120*, 12069.
[94] B. Schüpbach, A. Terfort, *Org. Biomol. Chem.* **2010**, *8*, 3552.
[95] K. T. Wong, T. S. Hung, Y. T. Lin, C. C. Wu, G. H. Lee, S. M. Peng, C. H. Chou, Y. L. O. Su, *Org. Lett.* **2002**, *4*, 513.
[96] M. Colombo, M. Giglio, I. Peretto, *J. Heterocycl. Chem.* **2008**, *45*, 1077.
[97] K. Heister, M. Zharnikov, M. Grunze, L. S. O. Johansson, A. Ulman, *Langmuir* **2001**, *17*, 8.
[98] K. Raiber, A. Terfort, C. Benndorf, N. Krings, H. H. Strehblow, *Surf. Sci.* **2005**, *595*, 56.
[99] J. F. Moulder, J. Chastain, *Handbook of X-Ray Photoelectron Spectroscopy: A Reference Book of Standard Spectra for Identification and Interpretation of XPS Data Physical Electronics Division*, Perkin-Elmer Corp., Eden Prairie, MN **1992**.
[100] J. Thome, M. Himmelhaus, M. Zharnikov, M. Grunze, *Langmuir* **1998**, *14*, 7435.
[101] H. Biebuyck, C. Bian, G. Whitesides, *Langmuir* **1994**, *10*, 1825.
[102] C. L. A. Lamont, J. Wilkes, *Langmuir* **1999**, *15*, 2037.
[103] F. Chesneau, B. Schüpbach, K. Szelągowska-Kunstman, N. Ballav, P. Cyganik, A. Terfort, M. Zharnikov, *Phys. Chem. Chem. Phys.* **2010**, *12*, 12123.
[104] H. Hamoudi, K. Döring, F. Chesneau, H. Lang, M. Zharnikov, *J. Phys. Chem. C* **2012**, *116*, 861.
[105] F. Schreiber, *Prog. Surf. Sci.* **2000**, *65*, 151.
[106] F. Chesneau, J. Zhao, C. Shen, M. Buck, M. Zharnikov, *J. Phys. Chem. C* **2010**, *114*, 7112.
[107] P. Batson, *Phys. Rev. B* **1993**, *48*, 2608.
[108] M. Domke, T. Mandel, A. Puschmann, C. Xue, D. A. Shirley, G. Kaindl, H. Petersen, P. Kuske, *Rev. Sci. Instrum.* **1992**, *63*, 80.
[109] M. J. Frisch, H. B. Schlegel, G. E. Scuseria, M. A. Robb, J. R. Cheeseman, G. Scalmani, V. Barone, B. Mennucci, G. A. Petersson, H. Nakatsuji, M. Caricato, X. Li, H. P. Hratchian, A. F. Izmaylov, J. Bloino, G. Zheng, J. L. Sonnenberg, M. Hada, M. Ehara, K. Toyota, R. Fukuda, J. Hasegawa, M. Ishida, T. Nakajima, Y. Honda, O. Kitao, H. Nakai, T. Vreven, J. A. J. Montgomery, J. E. Peralta, F. Ogliaro, M. Bearpark, J. J. Heyd, E. Brothers, K. N. Kudin, V. N. Staroverov, R. Kobayashi, J. Normand, K. Raghavachari, A. Rendell, J. C. Burant, S. S. Iyengar, J. Tomasi, M. Cossi, N. Rega, J. M. Millam, M. Klene, J. E. Knox, J. B. Cross, V. Bakken, C. Adamo, J. Jaramillo, R. Gomperts, R. E. Stratmann, O. Yazyev, A. J. Austin, R. Cammi, C. Pomelli, J. W. Ochterski, R. L. Martin, K. Morokuma, V. G. Zakrzewski, G. A. Voth, P. Salvador, J. J. Dannenberg, S. Dapprich, A. D. Daniels, Ö. Farkas, J. B. Foresman, J. V. Ortiz, J. Cioslowski, D. J. Fox, *Gaussian 09, Revision A. 02*, Gaussian, Inc., Wallingford, CT **2009**.
[110] J. Perdew, *Phys. Rev. B* **1986**, *33*, 8822.
[111] A. D. Becke, *Phys. Rev. A* **1988**, *38*, 3098.
[112] F. Weigend, R. Ahlrichs, *Phys. Chem. Chem. Phys.* **2005**, *7*, 3297.
[113] G. Kresse, J. Furthmuller, *Phys. Rev. B* **1996**, *54*, 11169.
[114] T. Bucko, J. Hafner, J. G. Angyan, *J. Chem. Phys.* **2005**, *122*, 124508.
[115] H. Monkhorst, J. Pack, *Phys. Rev. B* **1976**, *13*, 5188.
[116] G. Kresse, D. Joubert, *Phys. Rev. B* **1999**, *59*, 1758.
[117] J. P. Perdew, K. Burke, M. Ernzerhof, *Phys. Rev. Lett.* **1996**, *77*, 3865.
[118] A. Kokalj, *J. Mol. Graphics* **1999**, *17*, 176.
[119] L. Köhler, G. Kresse, *Phys. Rev. B* **2004**, *70*, 165405.
[120] Y. Shao, L. F. Molnar, Y. Jung, J. Kussmann, C. Ochsenfeld, S. T. Brown, A. T. B. Gilbert, L. V. Slipchenko, S. V. Levchenko, D. P. O'Neill, R. A. DiStasio Jr., R. C. Lochan, T. Wang, G. J. O. Beran, N. A. Besley, J. M. Herbert, C. Y. Lin, T. Van Voorhis, S. H. Chien, A. Sodt, R. P. Steele, V. A. Rassolov, P. E. Maslen, P. P. Korambath, R. D. Adamson, B. Austin, J. Baker, E. F. C. Byrd, H. Dachsel, R. J. Doerksen, A. Dreuw, B. D. Dunietz, A. D. Dutoi, T. R. Furlani, S. R. Gwaltney, A. Heyden, S. Hirata, C.-P. Hsu, G. Kedziora, R. Z. Khalliulin, P. Klunzinger, A. M. Lee, M. S. Lee, W.-Z. Liang, I. Lotan, N. Nair, B. Peters, E. I. Proynov, P. A. Pieniazek, Y. M. Rhee, J. Ritchie, E. Rosta, C. D. Sherrill, A. C. Simmonett, J. E. Subotnik, H. L. Woodcock III, W. Zhang, A. T. Bell, A. K. Chakraborty, D. M. Chipman, F. J. Keil, A. Warshel, W. J. Hehre, H. F. Schaefer III, J. Kong, A. I. Krylov, P. M. W. Gill, M. Head-Gordon, *Phys. Chem. Chem. Phys.* **2006**, *8*, 3172.
[121] T. H. J. Dunning Jr., *Chem. Phys.* **1989**, *90*, 1007.